PHILOSOPHICAL TRANSACTIONS A

royalsocietypublishing.org/journal/rsta

Research

Cite this article: Wang C, Wang Y, Wang Z-H, Yang X. 2025 Causal network and dynamic synchronization of urban thermal environment. *Phil. Trans. R. Soc. A* **383**: 20250041.
https://doi.org/10.1098/rsta.2025.0041

Received: 22 March 2025
Accepted: 5 June 2025

One contribution of 16 to a theme issue 'Urban heat spreading above and below ground'.

Subject Areas:
atmospheric science, climatology, meteorology, graph theory

Keywords:
urban heat, causality, complex network, dynamic synchronization, centrality, air temperature

Author for correspondence:
Chenghao Wang
e-mail: chenghao.wang@ou.edu

†These authors contributed equally to the study.

Electronic supplementary material is available online at https://doi.org/10.6084/m9.figshare.c.8039819.

THE ROYAL SOCIETY PUBLISHING

Causal network and dynamic synchronization of urban thermal environment

Chenghao Wang[1,2,†], Yihang Wang[3,†], Zhi-Hua Wang[3,†] and Xueli Yang[4]

[1]School of Meteorology, and [2]Department of Geography and Environmental Sustainability, University of Oklahoma, Norman, OK, USA
[3]School of Sustainable Engineering and the Built Environment, Arizona State University, Tempe, AZ, USA
[4]Scripps Institution of Oceanography, University of California San Diego, La Jolla, CA, USA

CW, 0000-0001-8846-4130; Z-HW, 0000-0001-9155-8605

Urban heat is a growing concern especially under global climate change and continuous urbanization. However, the understanding of its spatiotemporal propagation behaviours remains limited. In this study, we leverage a data-driven modelling framework that integrates causal inference, network topology analysis and dynamic synchronization to investigate the structure and evolution of temperature-based causal networks across the continental United States. We perform the first systematic comparison of causal networks constructed using warm-season daytime and nighttime air temperature anomalies in urban and surrounding rural areas. Results suggest strong spatial coherence of network links, especially during nighttime, and small-world properties across all cases. In addition, urban heat dynamics becomes increasingly synchronized across cities over time, particularly for maximum air temperature. Different network centrality measures consistently identify the Great Lakes region as a key mediator for spreading and mediating heat perturbations. This system-level analysis provides new insights into the spatial organization and dynamic behaviours of urban heat in a changing climate.

This article is part of the theme issue 'Urban heat spreading above and below ground'.

1. Introduction

Residents in cities are routinely exposed to elevated ambient air temperatures in comparison to their rural counterparts, a phenomenon well known as the canopy layer urban heat island (UHI) effect [1,2]. This excessive urban heat stress can be further exacerbated by the warming trend of global climate [3]. In the past few decades, increasing research efforts have focussed on numerically modelling and/or predicting UHI effects in major cities worldwide, primarily through various urban land surface models (LSMs), among which urban canopy models (UCMs) are particularly widely used for representing energy and water exchanges in urban areas [4,5].

Yet, it needs to be pointed out that urban LSMs are essentially process-based, driven by the physics of momentum, heat and scalar transport in the urban canopy layer through land–atmosphere interactions. Hence the vast majority of existing urban climate studies are site-specific or locality-based, typically restricted to local/neighbourhood and city scales [6]. In contrast, temperature variability and urban heat (along with other related environmental variables such as air pollution and precipitation) are rarely a local problem. Temperature (and humidity) states in one urban area can influence or be influenced by conditions in nearby or even remote cities. This is particularly evident in megacities and large urban clusters where atmospheric transport and shared synoptic weather patterns contribute to inter-city interactions [7,8].

Inter-city thermal interactions, without doubt, can be implicitly captured (to a certain degree) by regional weather and climate models incorporating urban LSMs. The strength of these models lies in their detailed representation of the underlying physics and their ability to simulate responses to specific atmospheric and surface conditions. However, such *process-based* modelling frameworks are inadequate to explicitly reveal the connectivity and directionality of influences among cities, especially those via relatively long-distance relationships, often referred to as teleconnections in large-scale climate systems [9,10]. To address this gap, recent efforts have proposed complex network analysis as an alternative, *system-based* approach to map the topology of inter-city connections. In early studies, the effective links between cities in an urban climate network were initially inferred using statistical correlation measures, such as the Pearson correlation coefficient [11,12]. Recognizing the limitations and potential spuriousness of correlation-based links, especially in systems driven by shared external forcing, causal inference methods, such as convergent cross mapping (CCM), have been introduced into urban climate network construction [13]. In these causal networks, effective links are measured by causal skills/influences that are physically more meaningful and interpretable with less spuriousness [14,15].

The construction of urban climate networks marks a transition towards system-based urban climate research (UHI effect included). For example, it allows for analysis of explicit topological features of urban climate maps (networks), such as hub–periphery structure, urban clustering, community properties and small-worldness [12], which are not readily accessible through convectional process-based urban climate modelling. In addition, key network metrics have been shown to predict abrupt and potentially catastrophic changes (critical transitions and tipping points) in urban climate dynamics, and could potentially serve as early warning signals that complement traditional statistical indicators such as variance and lag−1 autocorrelation [16,17]. Recent studies have also leveraged causal networks to identify regional mediators and meteorological factors that modulate the evolution of extreme urban heat waves [18,19]. Importantly, causal networks provide necessary strata upon which complex system dynamics operate, where interesting patterns can form, organize and evolve, such as causal emergence [20], synchronization [12] and system tipping [21]. Nonetheless, system-based approaches are often inherently data-driven and thus rely heavily on the availability, resolution and quality of long-term datasets that adequately capture urban climate signals. Furthermore, previous efforts have not fully explored key aspects of urban climate dynamics, such as urban–rural contrast,

differences between daytime and nighttime thermal dynamics and the integration of causal and dynamical systems perspectives.

In this study, we introduce a comprehensive data-driven modelling framework that integrates causal inference, network topology analysis and dynamic synchronization to investigate the structure and evolution of temperature-based climate networks across the contiguous U.S. (CONUS). Specifically, we aim to (i) characterize how network structure and connectivity differ between urban and surrounding rural areas, and between daytime and nighttime temperatures; (ii) identify pathways and regions that function as mediators in the propagation of temperature perturbations; and (iii) assess how synchronization of temperature dynamics among urban areas has evolved over time. This work represents the first systematic comparison between urban and rural causal climate networks derived from air temperature anomalies, which can offer a system-level perspective on the spatial organization, interconnectivity and dynamic evolution of urban heat, with important implications for climate risk assessment and heat mitigation strategies.

2. Methods

(a) Long-term time series of urban and rural air temperatures

Urban areas in this study are defined as densely populated areas with at least 50 000 inhabitants according to the U.S. Census Bureau [22]. For each of the 481 urban areas across the entire CONUS, we delineated the corresponding rural background as a buffer zone equal in area to the urban extent. To characterize the dynamics of urban heat and its rural counterpart during the warm season (May–September), we constructed a 40-year (1981–2020) time series of monthly average daily maximum and minimum near-surface air temperatures using two 1 km resolution datasets. For 2003–2020, we used a global daily dataset that integrates station measurements with satellite-based observations [23]. For the earlier period (1981–2002), we adopted the observation-based daily Daymet V4 dataset [24]. Since the Daymet dataset is known to underestimate urban heat signals [23,25], we further applied a bias correction using a modified quantile delta mapping method [26] with a three-month moving window for each day [27], leveraging the overlapping period (2003–2020) between these two high-resolution datasets. Further details of the bias correction approach can be found in a recent study [28]. The bias-corrected Daymet data were aggregated into monthly averages and merged with the post-2003 dataset to create a continuous time series. Note that all water bodies and other urban areas were removed before deriving the spatial averages of air temperature.

We then removed seasonal patterns by subtracting the long-term (40 year) climatological mean for each warm-season month from the corresponding monthly value for each urban/rural area. The resulting times series of monthly temperature anomalies serve as the basis for the subsequent CCM-based causal inference.

(b) Convergent cross mapping-based causal inference

The causal relationships between temperature anomalies were evaluated using the CCM method. The CCM method aims to detect causal interactions within nonlinear dynamic systems with weak-to-moderate couplings that are not purely stochastic. Compared to nonlinear correlation analysis, the CCM method provides as output asymmetrical causal strengths instead of symmetrical correlation coefficients between two variables, which enables the identification of directional causality. To determine the causations in dynamic systems, CCM looks for the signature of one variable in the time series of another variable. Specifically, it examines whether the time indices of nearby points on the manifold of one variable can be used to identify the nearby points on the manifolds of another. This can be achieved using simplex projection,

a nearest-neighbour estimating algorithm that applies exponentially weighted distances in state-space reconstruction [29].

Based on Takens' delay embedding theorem [30], the first step of the CCM method is to reconstruct the state-space trajectories (manifolds) of the variables in a dynamic system using time-lagged vectors. For X, the vector is given by $\mathbf{x}(t) = [X(t), X(t-\tau), \ldots, X(t-(E-1)\tau)]$, where τ is the time delay and E is the embedding dimension [29]. The time delay τ is typically determined based on the average oscillation period of the underlying time series of the targeted variable, while the value of the embedding dimension E can be obtained using the correlation integral and dimension method [13,31]. This method selects E as the smallest dimension beyond which the estimated correlation dimension no longer increases substantially, indicating that the attractor was sufficiently unfolded. Here, we selected $\tau = 1$ and $E = 3$ for temperature causal inference following a previous study [13].

To illustrate the CCM method, we use the canonical Lorenz system, a nonlinear dynamic system with three coupled variables, X, Y and Z. As shown in figure 1, the manifolds of the causally coupled variables, M_X and M_Y, are reconstructed from the aforementioned time-lagged vectors. When causal couplings exist between X and Y, there will be cross-mapping correspondence between M_X and M_Y. Then, we could estimate the time series of X from Y and vice versa. To make the cross-mapped estimate of $X(t)$, denoted as $\widehat{X}(t)$, we first identify the E+1 nearest neighbours of vector $\mathbf{y}(t)$ on the manifold M_Y, $\mathbf{y}(t_1)$, $\mathbf{y}(t_2)$, …, $\mathbf{y}(t_{E+1})$, since E+1 is the minimum number of points required for a bounded simplex in an E-dimensional space [32]. We use the time indices of these E+1 neighbours, t_1, t_2, …, t_{E+1}, to identify the corresponding putative neighbours in X, which are $X(t_1)$, $X(t_2)$, …, $X(t_{E+1})$. The estimated value of $X(t)$ is then calculated as a weighted average of these E+1 points,

$$\widehat{X}(t)\,|\,M_Y = \sum_{i=1}^{E+1} w_i(t) X(t_i), \tag{2.1}$$

where the weighting coefficients $w_i(t)$ are given by

$$w_i(t) = \frac{u_i(t)}{\sum_{j=1}^{E+1} u_j(t)}, \tag{2.2}$$

with

$$u_i(t) = \exp\left\{-\frac{\mathrm{d}[\mathbf{y}(t), \mathbf{y}(t_i)]}{\mathrm{d}[\mathbf{y}(t), \mathbf{y}(t_1)]}\right\}, \tag{2.3}$$

where $\mathrm{d}[\mathbf{y}(t), \mathbf{y}(t_i)]$ is the Euclidean distance between vectors $\mathbf{y}(t)$ and $\mathbf{y}(t_i)$ on M_Y.

Finally, to measure the causal influence of X on Y, we compute the correlation coefficient ρ between the estimated time series $\widehat{X}(t)\,|\,M_Y$ and the actual time series $X(t)$. This correlation coefficient, denoted as $\rho_{X|M_Y}$, serves as the causal strength and is calculated as

$$\rho_{X|M_Y} = \frac{\mathbf{E}\left\{[X(t) - \mu_X] \cdot \left[\widehat{X}(t)\,|\,M_Y - \mu_{\widehat{X}}\right]\right\}}{\sigma_X \sigma_{\widehat{X}}}, \tag{2.4}$$

where $\mathbf{E}$, μ and σ are the statistical expectation, mean and s.d., respectively. The causal strength from Y to X, $\rho_{Y|M_X}$, is defined similarly. Higher values of ρ indicate a stronger causal relationship between the variables.

We applied the CCM method separately to urban and rural temperature anomalies to assess the causal relationships among different areas. Specifically, we first conducted causal analysis over the full 40-year period to detect long-term climatological relationships. We also performed CCM within each of the 26 15-year moving windows (e.g. 1981–1995, 1982–1996, etc.) to investigate potential temporal variations.

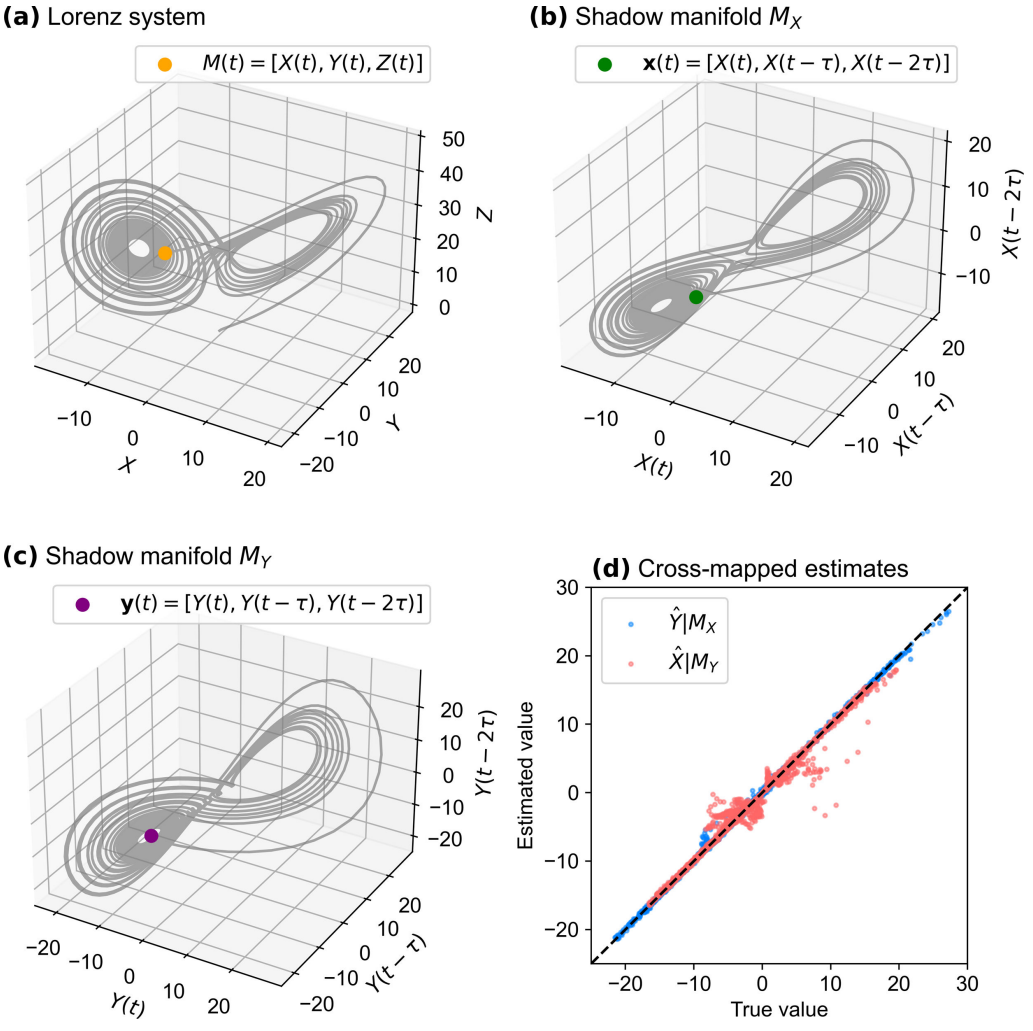

Figure 1. State-space reconstruction and causality analysis of the canonical Lorenz system using the convergent cross mapping (CCM) method: (a) the attractor manifold of the original system (M), (b) the shadow manifold M_X for variable X, (c) the shadow manifold M_Y for variable Y and (d) cross-mapped estimates of variables X and Y from CCM compared to their true values. The Lorenz system is governed by $\frac{dX}{dt} = 10(Y - X)$, $\frac{dY}{dt} = 28X - XZ - Y$, and $\frac{dZ}{dt} = XY - \frac{8}{3}Z$, where t is time. The embedding dimension $E = 3$, and the time delay $\tau = 5$.

(c) Construction of networks based on causal strength

The causal interactions identified through the CCM method can be represented topologically as directed networks [33], where nodes are individual urban (or rural) areas, and directed links/edges suggest the presence of causal influence from one area to another. In this study, we constructed unweighted causal networks by converting CCM-based causal strengths into binary values. This requires defining a threshold causal strength, ρ_{ths}, that determines whether a directed link exists or not. This threshold can be selected based on statistical significance or network topology [34]. We tested a series of ρ_{ths} values (figure 2 and electronic supplementary material, fig. S1) and selected an optimal threshold of 0.7 based on the following two criteria. First, the threshold value should ensure that the temperature network remains a single connected component (at least for most of the 15-year moving windows) rather than fragmenting into multiple disconnected components. Second, this value should be able to prioritize local and regional links while minimizing potentially spurious long-distance teleconnections.

Mathematically, the status of a directed link from node i to node j, A_{ij}, can be determined through a Heaviside step function [11],

$$A_{ij} = H(\rho_{ij} - \rho_{\text{ths}}), \tag{2.5}$$

where ρ_{ij} is the CCM-based causal strength from node i to node j.

All A_{ij} elements form the adjacency matrix $\mathbf{A}$, which can be used to classify links as unidirectional or bidirectional. A unidirectional link is defined when $A_{ij} = 1$ and $A_{ji} = 0$, or vice versa. A bidirectional link exists when $A_{ij} = A_{ji} = 1$, which indicates mutual causality between two areas. While bidirectional links appear as two directed links in the network, they are only counted once for link statistics in §3c.

To identify the dominant causal relationships in the constructed urban and rural networks, we define *dominant links* as those showing stronger causal strengths in one network (urban or rural) than the corresponding ones in the other network. For example, for each pair of urban areas i and j, we compare the CCM-based causal strength from i to j in the urban network, ρ_{ij}^{urban}, with that in the rural one, ρ_{ij}^{rural}. Then a directed link is considered a dominant link in the urban network if $\rho_{ij}^{\text{urban}} > \rho_{ij}^{\text{rural}}$. Similarly, a dominant link in the rural network is defined when $\rho_{ij}^{\text{rural}} > \rho_{ij}^{\text{urban}}$. Note that if a link exists only in one network (urban or rural), it is considered a dominant link in that network.

(d) Dynamic synchronization

The dynamic synchronization of the temperature-based causal networks is simulated using the Kuramoto model [35–37]. The original Kuramoto model was developed to simulate phase oscillators that interact with one another via sinusoidal coupling on a complete graph with all-to-all connection. The time evolution of each phase oscillator θ_i, representing an urban or rural area in this study, with natural frequency ω_i, is given by [35,36]

$$\dot{\theta}_i = \omega_i + \frac{K}{N}\sum_{j=1}^{N}\sin(\theta_j - \theta_i), \tag{2.6}$$

where the factor of $1/N$ is incorporated to ensure the convergency of the model at the thermodynamic limit of $N \to \infty$, N is the number of nodes and K is the coupling parameter that represents the strength of interaction between a pair of nodes.

To capture the dynamic synchronization in a real network, instead of a complete graph, the original Kuramoto model is modified to incorporate the adjacency matrices of realistic network connectivity [37–39],

$$\dot{\theta}_i = \omega_i + \sigma_K\sum_j A_{ij}\sin(\theta_j - \theta_i), \tag{2.7}$$

where σ_K is the coupling strength. The original Kuramoto is recovered by setting $\sigma_K = K/N$ and $A_{ij} = 1$, $\forall i \neq j$.

The intrinsic frequency ω usually follows a unimodal, symmetric probability density function $g(\omega)$, centred around a mean frequency Ω (e.g. the dominant diurnal frequency of temperature variations). Without loss of generality, we set $\Omega = 0$ given the rotational symmetry, such that $g(\omega) = g(-\omega)$. Here, we specify that $g(\omega)$ follows a random Lorentzian/Cauchy probability density function,

$$g(\omega) = \frac{\gamma}{\pi(\gamma^2 + \omega^2)}, \tag{2.8}$$

where γ is the scale parameter.

To describe the steady state to which the temporal evolution of a causal network will converge, we define a complex order parameter r that measures the system dynamics of all nodes [37],

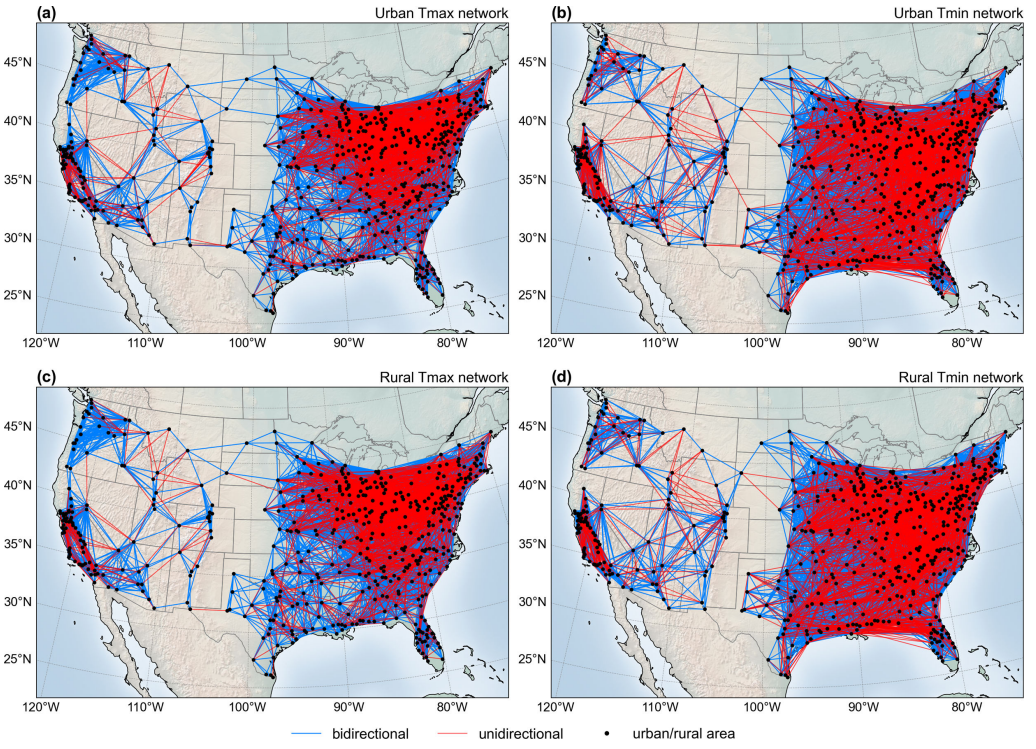

Figure 2. Temperature-based 40-year causal networks constructed based on (a) urban maximum air temperature, (b) urban minimum air temperature, (c) rural maximum air temperature and (d) rural minimum air temperature with a causal strength threshold of 0.7.

$$r(t)e^{i\phi(t)} = \frac{1}{N}\sum_{j=1}^{N} e^{i\theta_j(t)}, \tag{2.9}$$

where $0 \le r \le 1$ measures the phase coherence of all nodes, with $r = 0$ indicating complete incoherence and $r = 1$ suggesting phase locking, and ϕ is the average phase. More interestingly, real-world networks often settle into a steady state with $0 < r < 1$ in which a subset of oscillators synchronize while others remain drifting. This behaviour is analogous to criticality or phase transitions in complex systems [40].

Using the order parameter defined above, the original Kuramoto model reduces to [37]

$$\dot{\theta}_i = \omega_i + Kr\sin(\phi - \theta_i). \tag{2.10}$$

A critical coupling strength K_c exists, above which the network transitions to a synchronized state. The value of K_c, as a function of $g(\omega)$, can be analytically determined by the self-consistency condition [41],

$$K_c = \frac{2}{\pi g(0)}. \tag{2.11}$$

In the case of the modified Kuramoto model for a real complex network, i.e. equation (2.7), finding the critical coupling strength is more challenging, and analytical solutions for K_c are in general intractable. As a result, in this study, we determine K_c empirically through sensitivity experiments (figure 3a).

Beyond the order parameter r, the converged states of dynamic synchronization can also be described using the network (system) potential υ [42],

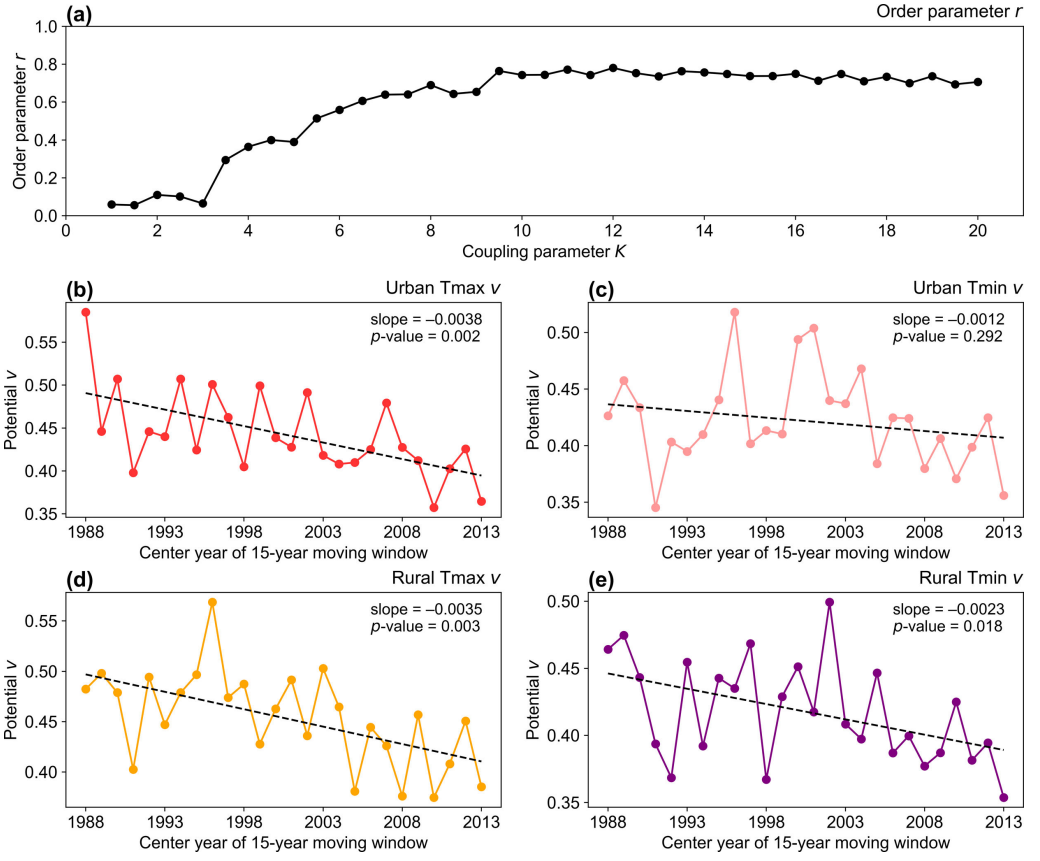

Figure 3. Synchronization of causal networks simulated using the Kuramoto model: (a) order parameter r as a function of the coupling parameter K, and the temporal variability of system potential υ for networks with $K = 10$ based on (b) urban maximum air temperature, (c) urban minimum air temperature, (d) rural maximum air temperature and (e) rural minimum air temperature. The dashed lines in (b)–(e) are linear regression fits to system potential.

$$\upsilon = \frac{4}{N^2}\sum_i \sum_{j>i} \sin^2\left(\frac{\theta_j - \theta_i}{2}\right). \tag{2.12}$$

This measure is normalized by the factor $4/N^2$ to $0 < \upsilon < 1$, which provides an alternative representation of synchronization. By taking the partial derivative, the ordinary differential equation of Kuramoto model can be re-constructed as [42]

$$\dot{\theta}_i - \omega_i = -\frac{KN}{2}\frac{\partial \upsilon}{\partial \theta_i}. \tag{2.13}$$

Analytically, it has been shown [12] that the order parameter r and the system potential υ are related by

$$\upsilon + r^2 = 1. \tag{2.14}$$

This suggests an inverse relationship between r and υ: as synchronization and order parameter r increase, the system potential υ decreases and vice versa. In other words, mathematically, equation (2.13) represents a gradient system, where υ represents the potential energy of the synchronization basin with a coupling strength of K [43].

(e) Centrality measures

Centrality quantifies the importance of each node (urban or rural area herein) based on its position and topological relationships with other nodes in a network [33]. Centrality analysis can help distinguish nodes and regions that play a dominant role in shaping the structure and dynamics of temperature causal networks. Here, we adopted PageRank centrality to quantify the relative importance of each urban/rural area. PageRank centrality was originally developed to rank web pages based on the structure of hyperlinks [44]. The PageRank centrality of a node depends on both the number of nodes that link to it (i.e. incoming links) and the PageRank centrality of these nodes. Therefore, in a causal network, a node receives a high PageRank centrality value if it is causally influenced by many other influential nodes. PageRank centrality of node i, PR_i, can be calculated iteratively as [44]

$$PR_i = \frac{1-d}{N} + d\sum_j \frac{PR_j}{k_j^{\text{out}}}, \tag{2.15}$$

where d is the damping factor that is typically set to 0.85 and k_j^{out} is the out-degree of node j that links to node i.

We also used another centrality measure, DomiRank centrality [45], to assess node importance in our networks. Unlike PageRank centrality, DomiRank centrality measures a node's dominance over its immediate neighbours. As a result, A high DomiRank centrality value suggests that a node is surrounded by less influential nodes. Compared to other centrality measures, it has been demonstrated to be more effective in identifying critical nodes whose removal (i.e. targeted attacks) would effectively disrupt network structure. The DomiRank centrality of node i, DR_i, in an unweighted network is defined as the steady-state solution of the following dynamical process [45]:

$$\frac{\mathrm{d}DR_i(t)}{\mathrm{d}t} = \alpha\sum_j\left[\delta - DR_j(t)\right] - \beta DR_i(t), \tag{2.16}$$

where DR_j is the DomiRank of node j connected to node i, α is a proportionality constant representing the degree of competition among neighbouring nodes, β is a constant representing the rate of natural relaxation and δ is the threshold for domination. Equation (2.16) can be recursively solved. Without loss of generality, we set $\eta = \frac{\alpha}{\beta}$, $\beta = 1$ and $\delta = 1$ [45], which leads to the following discrete-time update rule:

$$DR_i(t+\Delta t) = DR_i(t) + \Delta t\left\{\eta\sum_j\left[1 - DR_j(t)\right] - DR_i(t)\right\}. \tag{2.17}$$

An optimal η value is numerically selected as the one that generates the most effective attack and leads to the largest fragmentation of the network.

3. Results and discussion

(a) Structure and evolution of causal networks

As shown in figure 2, the 40-year causal networks constructed based on air temperature in urban and rural areas exhibit a strong prevalence of bidirectional causal relationships, a sign of widespread mutual interactions among different areas. Bidirectional links account for 86.2%, 86.9%, 86.4% and 87.2% of all connections in the networks based on urban maximum temperature, urban minimum temperature, rural maximum temperature and rural minimum temperature, respectively. Note that here two directed links between the same pair of nodes are counted as one, as mentioned in §2c. In addition, urban and rural networks based on minimum air

temperature contain approximately 26% more links than their maximum temperature counterparts. This suggests a relatively stronger spatial coherence for minimum air temperature.

For spatial patterns, higher concentrations of causal links are observed in the eastern and western U.S., with far fewer links in the central part of the country. The highest densities of causal links appear around the Great Lakes and northeastern U.S., where both urban and rural areas exhibited strong temperature interdependencies. The comparison among networks based on different causal strength thresholds (figure 2 and electronic supplementary material, fig. S1) reveals a clear hierarchical structure [8,12,46]. With increasing threshold values, weaker, long-distance connections spanning multiple states disappear (e.g. links between southern California and Colorado). However, certain clusters with strong intra-regional connections remain even under very high threshold values, especially in California's Central Valley, the Great Lakes region, the upper Southeast and northeastern U.S. (electronic supplementary material, fig. S1c,d). This persistent regional coherence implies high-strength causal interactions that are driven by shared background climates and similar land–atmosphere interactions, while also partially influenced by the spatial distribution of nodes.

Despite year-to-year variations, the structural characteristics of 15-year urban and rural causal networks (electronic supplementary material, figs. S2–S5) generally remain consistent over time, with patterns resembling those of the 40-year networks. Nevertheless, the total number of causal links increased over time (electronic supplementary material, fig. S6), especially for those based on urban minimum air temperature, signalling a progressive strengthening of interdependency in temperature dynamics among different areas [47]. This trend is probably influenced in part by the intensifying UHI effect, as continued urban development has led to similar changes in surface energy balance characteristics, such as increased heat retention. As a result, warming patterns have become more similar across cities, increasing the causal connectivity across networks. This enhanced connectivity is also reflected by the transition from fragmented networks with multiple components in earlier years to those with a single connected component in recent years. To quantify this transition, here we use the average shortest path length of the largest component in the causal network, which measures the average number of hops along the shortest paths for all pairs of nodes [33]. For all four sets of 15-year networks, the average shortest path length has experienced a statistically significant ($p < 0.1$) decline over time (table 1).

Interestingly, all causal networks analysed in this study have an average shortest path length of approximatley 5, a characteristic of the small-world effect that has been observed in many real-world networks [48,49]. This characteristic implies that temperature anomalies among urban (or rural) areas are not only closely interconnected, but can also efficiently propagate across the network with few intermediate steps. Similar co-existence of local clustering and global connectivity has been reported in a previous study using correlation-based networks among U.S. cities [12].

(b) Characteristics of dynamic synchronization

In this study, we assume that the initial phases of all oscillators ($n = 481$) in the Kuramoto model follow a random Lorentzian distribution as specified in equation (2.8), with $\gamma = 0.5$. The critical coupling strength is empirically determined, as shown in figure 3a. Results suggest that when $K > K_c \cong 8.5$, all temperature-based networks become uniformly synchronizable, with the order parameter r stabilizing around 0.75. As a result, we set $K = 10$ for all subsequent simulations.

Figure 3b–e shows the temporal evolution of the system potential υ for the four sets of causal networks constructed using 15-year moving windows. Overall, υ values range between 0.35 and 0.58, showing a decreasing trend over time for all cases. In comparison, the base potential υ_0, with the initial phases of all oscillators ω_i following the random Lorentzian distribution, is 0.60 for all networks. This indicates that the Kuramoto model predicts convergence of the major components of all causal networks towards synchronized states rather than drifting away. In

Table 1. Average shortest path length of the largest component of the causal networks.

	urban maximum air temperature	rural maximum air temperature	urban minimum air temperature	rural minimum air temperature
40-year causal networks	5.08	4.53	5.17	4.83
15-year causal networks	5.24 ± 0.56	5.26 ± 0.54	4.90 ± 1.08	4.91 ± 1.07
trend in 15-year causal networks ($year^{-1}$)	-0.034 ($p = 0.015$)	-0.026 ($p = 0.065$)	-0.067 ($p = 0.015$)	-0.085 ($p = 0.001$)

general, networks based on maximum temperature anomalies for both urban and rural areas exhibit more significant decreasing trends in υ than their minimum temperature counterparts. This implies that the most critical daytime thermal environment of CONUS cities (and their rural surroundings) is becoming increasingly synchronizable, potentially driven by enhanced long-range and synoptic-scale advection. In other words, this reflects a stronger tendency for urban areas to respond in a coordinated manner to large-scale temperature perturbations, which may contribute to more widespread extreme heat events. In contrast, the nocturnal thermal environment remains relatively 'localized', owing to the suppression of turbulent transport at night [50].

In addition, the decrease in network potential υ (hence the increase in order parameter r) over the 40-year period suggests that interactions among CONUS cities in the causal networks are strengthening and approaching a more synchronized state. This suggests the potential influence of changes in regional to global climate patterns, as supported by recent findings that the variability of causal strengths in urban hydroclimate networks agrees well with global climate oscillations such as El Niño–Southern Oscillation [51]. This ubiquitous trend of increasing synchronizability has a profound implication for the emergence of future urban climate patterns in the U.S. A possible consequence is the potential increase in the frequency/intensity of climatic extremes. For example, heat waves may begin to affect more cities simultaneously with greater severity, owing to the enhanced synergy (and therefore synchronization) of temperature dynamics across the urban climate network [12].

(c) Temporal evolution of dominant links

The temporal evolution of dominant links in urban and rural networks suggests distinct patterns over the past four decades (figure 4). The total number of rural dominant links remains relatively stable, with only a slight decrease in bidirectional ones, especially after the late 1990s (around 1998–2000). In comparison, the total number of urban dominant links increases over time, a trend that holds for both unidirectional and bidirectional ones. As a result, while urban dominant links were initially fewer than rural ones, they surpassed them around 2004. These trends suggest that urban areas are increasingly interconnected in terms of dynamics in temperature anomalies. This is a collective result of similar urban surface energy partitioning and, in particular, enhanced nocturnal UHI effect, consistent with the more rapid urban warming than rural surroundings observed in previous studies [52,53].

This growing interdependency among urban areas also indicates that cities exert increasingly strong causal influences on one another over time. A recent study demonstrates that megacities are not only causally connected with other cities but can also act as pacemakers that regulate the structure of urban climate networks during heat waves [18]. Therefore, in climate analysis, urban areas should be treated as components of larger, dynamically linked networks rather than isolated entities. Similarly, regionally coordinated urban heat mitigation approaches are needed to account for the spatially interconnected nature of urban heat dynamics. With

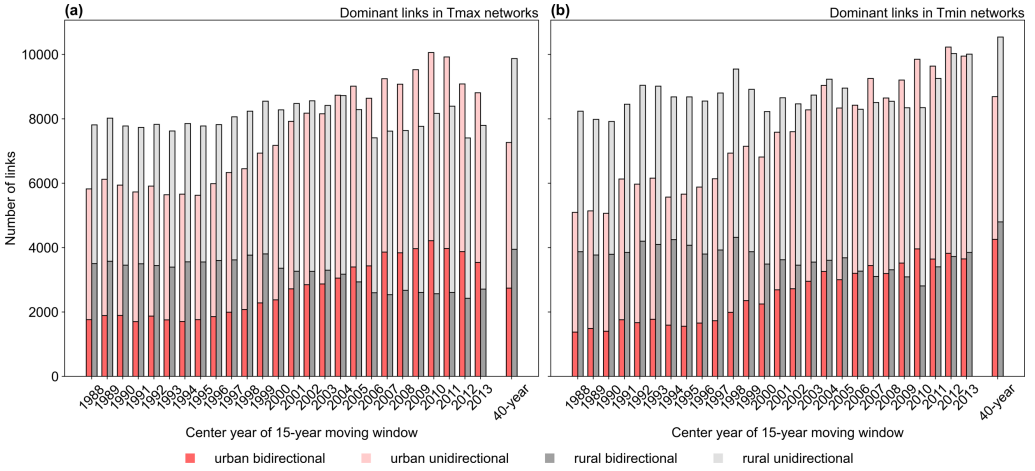

Figure 4. Number of dominant links in the 40-year and 15-year networks based on (a) maximum air temperature and (b) minimum air temperature.

continuous urbanization and climate change, such collaborative planning at regional scales will become increasingly necessary for reducing urban heat risks.

(d) Patterns of network centrality

PageRank centrality analysis identifies three key regions with consistently stronger influence across all four 40-year causal networks (figure 5): the Great Lakes region, California's Central Valley and north Texas. This regional patterns align with those observed in previous event-based urban climate networks constructed based on hourly temperature data [18], suggesting that these regions may serve as major hubs of causal influence for temperature anomalies. However, differences exist between maximum and minimum temperature-based networks. The Great Lakes region and north Texas show higher normalized PageRank values in maximum temperature-based networks, whereas Central valley has relatively higher values in minimum temperature-based ones. This discrepancy is potentially due to the differences in daytime and nocturnal land–atmosphere interactions and boundary-layer dynamics. For example, the higher PageRank values for minimum temperature-based networks in Central Valley may reflect the role of nighttime heat retention and topography in this agriculturally intensive region [54,55].

DomiRank centrality based on 40-year causal networks exhibits a slightly different spatial pattern (electronic supplementary material, fig. S7). While it also suggests the Great Lakes region as a key area, DomiRank centrality results bifurcate this region into two distinct zones. This is mainly because of the DomiRank centrality's implicit competition mechanism, which can produce more disparate centrality values among connected nodes compared to PageRank [45]. The consistency between these two centrality measures further highlights the importance of the Great Lakes region. In fact, this region has been suggested to function as a causal gateway that spreads and mediates perturbations of heat, drought and precipitation [13,34,56]. This is also evident in figure 2, where the Great Lakes region is much more densely connected than other regions. In addition, unlike PageRank that remains stable across all 15-year networks, DomiRank centrality shows a greater year-to-year variability, which leads to slight differences between the 40-year network results and the long-term averages of the 15-year networks (electronic supplementary material, figs. S8 and S9). Nevertheless, the Great Lakes region remains a dominant feature that regulates urban heat interactions in all 15-year networks.

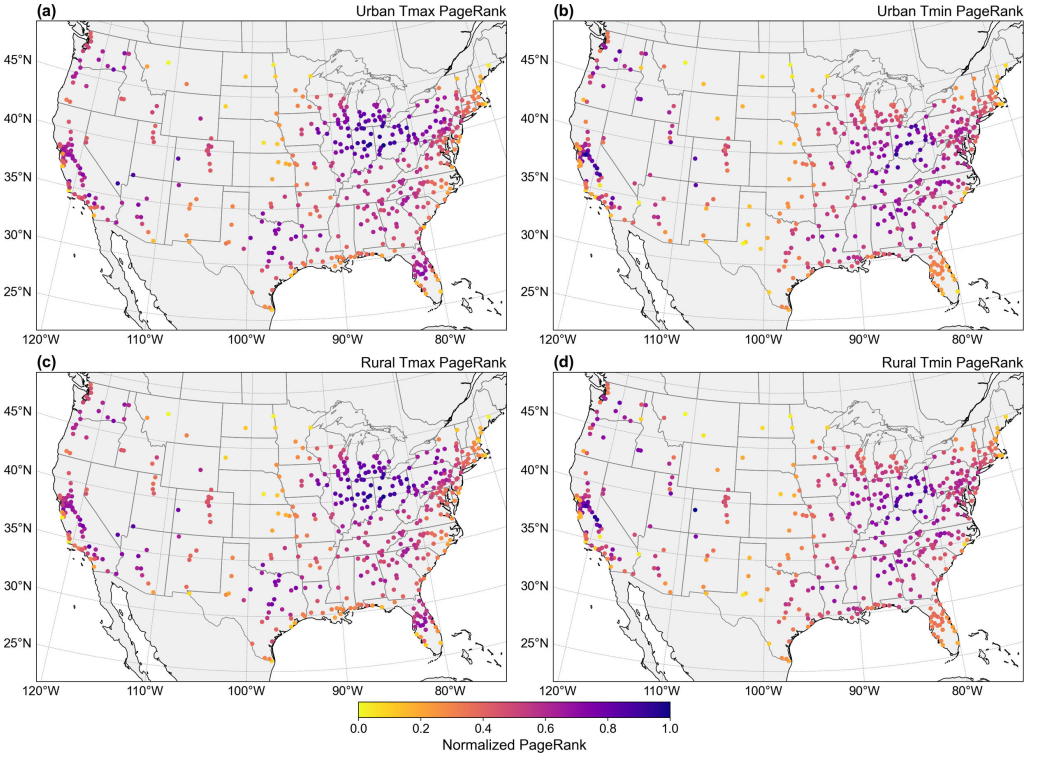

Figure 5. Normalized PageRank centrality for 40-year causal networks constructed based on (a) urban maximum air temperature, (b) urban minimum air temperature, (c) rural maximum air temperature and (d) rural minimum air temperature. Centrality values in each network are normalized using maximum and minimum values.

4. Conclusions

In this study, we investigated the structure and dynamics of causal networks constructed based on maximum and minimum air temperatures during warm seasons in CONUS urban areas and their rural backgrounds. The spatial distribution of directed links in networks suggests stronger spatial coherence during nighttime, with the highest densities of causal links in the Great Lakes region and northeastern U.S. In addition, networks have become increasingly dense over time, especially those based on urban minimum air temperature. This strengthened interdependency in temperature dynamics among different areas is probably influenced by the intensified UHI effect. All networks exhibit the small-world effect with co-existence of local clustering and global connectivity, which allows temperature perturbations to propagate efficiently across different areas. Our dynamic synchronization analyses demonstrate the increasing synchronizability among urban areas, particularly in networks based on maximum air temperature. The evolution of dominant links in urban and rural causal networks reveals that urban areas are increasingly interconnected in terms of temperature anomalies, owing to both similar urban surface energy balance characteristics and enhanced nocturnal UHI effect. Network centrality measures further highlight the Great Lakes region as a key mediator for spreading and mediating heat perturbations.

We acknowledge that the similarity between urban and rural networks may result from the effect of urban areas on their immediate rural surroundings, especially when using air temperature influenced by advection. Nevertheless, the selection of immediate rural surroundings here remains a practical and reliable approach for minimizing the confounding effects of topography. Our analysis also depends on the quality and spatial resolution of the underlying

air temperature dataset, and the use of monthly anomalies may smooth out daily to sub-daily processes that are more relevant for characterizing urban heat exposure and informing mitigation. Despite these limitations, the findings of this study emphasize the importance of considering urban areas and their rural surroundings as dynamically linked systems in climate analysis. For megacities with high centrality (e.g. Chicago), synchronized temperature dynamics with surrounding areas may exacerbate heat stress experienced by nearby cities. In addition, this interconnectivity highlights the potential for heat mitigation strategies implemented in one city to influence nearby areas, suggesting the need for coordinated planning at metropolitan and regional scales to maximize benefits. While this study demonstrates the feasibility of the data-driven modelling framework, translating these insights into climate-sensitive design and decision-making will require sub-city scale analyses and integration with numerical simulations of specific heat mitigation strategies. It is important to note that, given the overall relatively stagnant urbanization rate in the U.S. in the past decades, we speculate that the observed increase in synchronizability is more attributable to changes in background climate than by urban expansion and/or increased urban anthropogenic activities. Therefore, it would be of great interest to apply this data-driven modelling framework to rapidly urbanizing regions, such as China, India and major African cities.

Data accessibility. Access to data and code used in this study can be found in the supplementary material [57].

Declaration of AI use. We have not used AI-assisted technologies in creating this article.

Authors' contributions. C.W.: conceptualization, data curation, formal analysis, funding acquisition, investigation, methodology, project administration, resources, software, supervision, validation, visualization, writing—original draft; Y.W.: data curation, formal analysis, investigation, methodology, software, validation, writing—original draft; Z.W.: conceptualization, formal analysis, funding acquisition, investigation, methodology, resources, software, validation, visualization, writing—original draft; X.Y.: methodology, validation, writing—review and editing.

All authors gave final approval for publication and agreed to be held accountable for the work performed therein.

Conflict of interest declaration. We declare we have no competing interests.

Funding. This work was supported by the U.S. National Science Foundation (NSF) under grant numbers OIA-2327435 and CNS-2301858, the National Aeronautics and Space Administration (NASA) under grant numbers 80NSSC24K1056 (Early Career Investigator Program in Earth Science) and 80NSSC24K0357, and the U.S. Geological Survey (USGS) under grant number G24AC00475. Z.H.W. and Y.W. were supported by the U.S. NSF under grant number AGS-2300548. The contents of this work are solely the responsibility of the authors and do not necessarily represent the views of the South Central Climate Adaptation Science Center or the USGS. This manuscript is submitted for publication with the understanding that the U.S. Government is authorized to reproduce and distribute reprints for Governmental purposes.

References

1. Oke TR. 1973 City size and the urban heat island. *Atmos. Environ. (1967)* **7**, 769–779. (doi:10.1016/0004-6981(73)90140-6)
2. Oke TR. 1982 The energetic basis of the urban heat island. *Q. J. R. Meteorol. Soc.* **108**, 1–24. (doi:10.1002/qj.49710845502)
3. IPCC. 2021 *Climate change 2021: The physical science basis. Contribution of Working Group I to the Sixth Assessment Report of the Intergovernmental Panel on Climate Change*. Cambridge, UK and New York, NY, USA: Cambridge University Press.
4. Grimmond CSB *et al*. 2010 The international urban energy balance models comparison project: first results from Phase 1. *J. Appl. Meteor. Clim.* **49**, 1268–1292. (doi:10.1175/2010JAMC2354.1)
5. Lipson MJ *et al*. 2024 Evaluation of 30 urban land surface models in the Urban - PLUMBER project: Phase 1 results. *Q. J. R. Meteorol. Soc.* **150**, 126–169. (doi:10.1002/qj.4589)
6. Wang ZH. 2022 Reconceptualizing urban heat island: beyond the urban-rural dichotomy. *Sustain. Cities Soc.* **77**, 103581. (doi:10.1016/j.scs.2021.103581)

7. Lowry WP. 1977 Empirical estimation of urban effects on climate: a problem analysis. *J. Appl. Meteorol.* **16**, 129–135. (doi:10.1175/1520-0450(1977)0162.0.co;2)
8. Wang C, Wang ZH, Li Q. 2020 Emergence of urban clustering among U.S. cities under environmental stressors. *Sustain. Cities Soc.* **63**, 102481. (doi:10.1016/j.scs.2020.102481)
9. Li X *et al*. 2021 Tropical teleconnection impacts on Antarctic climate changes. *Nat. Rev. Earth Environ.* **2**, 680–698. (doi:10.1038/s43017-021-00204-5)
10. Liu T *et al*. 2023 Teleconnections among tipping elements in the Earth system. *Nat. Clim. Chang.* **13**, 67–74. (doi:10.1038/s41558-022-01558-4)
11. Wang C, Wang ZH. 2020 A network-based toolkit for evaluation and intercomparison of weather prediction and climate modeling. *J. Environ. Manag.* **268**, 110709. (doi:10.1016/j.jenvman.2020.110709)
12. Wang ZH, Wang C, Yang X. 2021 Dynamic synchronization of extreme heat in complex climate networks in the contiguous United States. *Urban Clim.* **38**, 100909. (doi:10.1016/j.uclim.2021.100909)
13. Yang X, Wang ZH, Wang C, Lai YC. 2022 Detecting the causal influence of thermal environments among climate regions in the United States. *J. Environ. Manag.* **322**, 116001. (doi:10.1016/j.jenvman.2022.116001)
14. Runge J. 2018 Causal network reconstruction from time series: from theoretical assumptions to practical estimation. *Chaos* **28**, 075310. (doi:10.1063/1.5025050)
15. Runge J *et al*. 2015 Identifying causal gateways and mediators in complex spatio-temporal systems. *Nat. Commun.* **6**, 8502. (doi:10.1038/ncomms9502)
16. Scheffer M *et al*. 2009 Early-warning signals for critical transitions. *Nature* **461**, 53–59. (doi:10.1038/nature08227)
17. Yang X, Wang ZH, Wang C. 2022 Critical transitions in the hydrological system: early-warning signals and network analysis. *Hydrol. Earth Syst. Sci.* **26**, 1845–1856. (doi:10.5194/hess-26-1845-2022)
18. Yang X, Wang ZH, Wang C, Lai YC. 2024 Megacities are causal pacemakers of extreme heatwaves. *npj Urban Sustain.* **4**, 8. (doi:10.1038/s42949-024-00148-x)
19. Wang Y, Yang X, Wang ZH. 2024 Causal mediation of urban temperature by geopotential height in U.S. cities. *Sustain. Cities Soc.* **100**, 105010. (doi:10.1016/j.scs.2023.105010)
20. Varley TF, Hoel E. 2022 Emergence as the conversion of information: a unifying theory. *Philos. Trans. R. Soc. A* **380**, 20210150. (doi:10.1098/rsta.2021.0150)
21. Panahi S, Do Y, Hastings A, Lai YC. 2023 Rate-induced tipping in complex high-dimensional ecological networks. *Proc. Natl Acad. Sci. USA* **120**, e2308820120. (doi:10.1073/pnas.2308820120)
22. United States Census Bureau. 2021 *TIGER/Line Shapefiles: Technical Documentation*. p. 172. U.S. Census Bureau. See https://www2.census.gov/geo/pdfs/maps-data/data/tiger/tgrshp2021/TGRSHP2021_TechDoc.pdf.
23. Zhang T, Zhou Y, Zhao K, Zhu Z, Chen G, Hu J, Wang L. 2022 A global dataset of daily maximum and minimum near-surface air temperature at 1 km resolution over land (2003–2020). *Earth Syst. Sci. Data* **14**, 5637–5649. (doi:10.5194/essd-14-5637-2022)
24. Thornton PE, Shrestha R, Thornton M, Kao SC, Wei Y, Wilson BE. 2021 Gridded daily weather data for North America with comprehensive uncertainty quantification. *Sci. Data* **8**, 190. (doi:10.1038/s41597-021-00973-0)
25. Thompson L, Wang C, He C, Lin TS, Liu C, Dudhia J. 2025 Assessment of convection-permitting hydroclimate modeling in urban areas across the contiguous United States. *Urban Clim.* **61**, 102375. (doi:10.1016/j.uclim.2025.102375)
26. Cannon AJ, Sobie SR, Murdock TQ. 2015 Bias correction of GCM precipitation by quantile mapping: how well do methods preserve changes in quantiles and extremes? *J. Clim.* **28**, 6938–6959. (doi:10.1175/jcli-d-14-00754.1)
27. Wang C *et al*. 2023 Impacts of climate change, population growth, and power sector decarbonization on urban building energy use. *Nat. Commun.* **14**, 6434. (doi:10.1038/s41467-023-41458-5)
28. Wang C, Hu XM, Feron S, Leffel J, Cordero RR. 2025 Compound heat and ozone pollution in the urban environment. *Urban Clim.* **62**, 102511. (doi:10.1016/j.uclim.2025.102511)
29. Sugihara G, May R, Ye H, Hsieh C hao, Deyle E, Fogarty M, Munch S. 2012 Detecting causality in complex ecosystems. *Science* **338**, 496–500. (doi:10.1126/science.1227079)

30. Floris T. 1981 Detecting strange attractors in turbulence (eds DA Rand, LS Young, DA Rand, LS Young). In *Dynamical systems and turbulence, warwick 1980: proceedings of a symposium held at the university of warwick 1979/80*, pp. 366–381. Berlin, Germany: Springer. (doi:10.1007/BFb0091924)
31. Jiang JJ, Huang ZG, Huang L, Liu H, Lai YC. 2016 Directed dynamical influence is more detectable with noise. *Sci. Rep.* **6**, 24088. (doi:10.1038/srep24088)
32. Sugihara G, May RM. 1990 Nonlinear forecasting as a way of distinguishing chaos from measurement error in time series. *Nature* **344**, 734–741. (doi:10.1038/344734a0)
33. Newman MEJ. 2018 *Networks*, 2nd edn. Oxford, UK: Oxford University Press.
34. Yang X, Wang Z, Wang C, Lai Y. 2023 Finding causal gateways of precipitation over the contiguous United States. *Geophys. Res. Lett.* **50**, L101942. (doi:10.1029/2022gl101942)
35. Kuramoto Y. 1975 Self-entrainment of a population of coupled non-linear oscillators (ed. H Araki). In *International Symposium on Mathematical Problems in Theoretical Physics*, pp. 420–422. Berlin, Germany: Springer. (doi:10.1007/BFb0013365)
36. Kuramoto Y. 1984 *Chemical oscillations, waves, and turbulence*. Berlin, Germany: Springer. (doi:10.1007/978-3-642-69689-3)
37. Acebrón JA, Bonilla LL, Pérez Vicente CJ, Ritort F, Spigler R. 2005 The Kuramoto model: a simple paradigm for synchronization phenomena. *Rev. Mod. Phys.* **77**, 137–185. (doi:10.1103/RevModPhys.77.137)
38. Arenas A, Díaz-Guilera A, Kurths J, Moreno Y, Zhou C. 2008 Synchronization in complex networks. *Phys. Rep.* **469**, 93–153. (doi:10.1016/j.physrep.2008.09.002)
39. Rodrigues FA, Peron TKDM, Ji P, Kurths J. 2016 The Kuramoto model in complex networks. *Phys. Rep.* **610**, 1–98. (doi:10.1016/j.physrep.2015.10.008)
40. Muñoz MA. 2018 Criticality and dynamical scaling in living systems. *Rev. Mod. Phys.* **90**, 031001. (doi:10.1103/RevModPhys.90.031001)
41. Strogatz SH. 2000 From Kuramoto to Crawford: exploring the onset of synchronization in populations of coupled oscillators. *Phys. D* **143**, 1–20. (doi:10.1016/s0167-2789(00)00094-4)
42. Rajapakse I, Smale S. 2017 The Pitchfork Bifurcation. *Int. J. Bifurcation Chaos* **27**, 1750132. (doi:10.1142/S0218127417501322)
43. Wiley DA, Strogatz SH, Girvan M. 2006 The size of the sync basin. *Chaos* **16**, 015103. (doi:10.1063/1.2165594)
44. Brin S, Page L. 1998 The anatomy of a large-scale hypertextual Web search engine. *Comput. Networks ISDN Syst.* **30**, 107–117. (doi:10.1016/S0169-7552(98)00110-X)
45. Engsig M, Tejedor A, Moreno Y, Foufoula-Georgiou E, Kasmi C. 2024 DomiRank centrality reveals structural fragility of complex networks via node dominance. *Nat. Commun.* **15**, 56. (doi:10.1038/s41467-023-44257-0)
46. Ravasz E, Barabási AL. 2003 Hierarchical organization in complex networks. *Phys. Rev. E* **67**, 026112. (doi:10.1103/physreve.67.026112)
47. Li Y, Schubert S, Kropp JP, Rybski D. 2020 On the influence of density and morphology on the Urban Heat Island intensity. *Nat. Commun.* **11**, 2647. (doi:10.1038/s41467-020-16461-9)
48. Watts DJ, Strogatz SH. 1998 Collective dynamics of 'small-world' networks. *Nature* **393**, 440–442. (doi:10.1038/30918)
49. Tsonis AA, Swanson KL, Roebber PJ. 2006 What do networks have to do with climate? *Bull. Am. Meteorol. Soc.* **87**, 585–596. (doi:10.1175/BAMS-87-5-585)
50. Stull RB. 1988 *An introduction to boundary layer meteorology*. Dordrecht, The Netherlands: Springer Netherlands. See https://link.springer.com/book/10.1007/978-94-009-3027-8.
51. Yang X, Wang ZH, Li Q, Lai YC. 2024 Time variability and periodicities of cross‐regional hydroclimatic causation in the contiguous United States. *Q. J. R. Meteorol. Soc.* **150**, 3942–3956. (doi:10.1002/qj.4800)
52. Yang X, Hou Y, Chen B. 2011 Observed surface warming induced by urbanization in east China. *J. Geophys. Res.* **116**, D015452. (doi:10.1029/2010jd015452)
53. Liu Z *et al*. 2022 Surface warming in global cities is substantially more rapid than in rural background areas. *Commun. Earth Environ.* **3**, 219. (doi:10.1038/s43247-022-00539-x)
54. Bianco L, Djalalova K IV, Wilczak C. 2011 Diurnal evolution and annual variability of boundary-layer height and its correlation to other meteorological variables in California's Central Valley. *Bound. Layer Meteorol.* **140**, 491–511. (doi:10.1007/s10546-011-9622-4)

55. Kueppers LM, Snyder MA. 2012 Influence of irrigated agriculture on diurnal surface energy and water fluxes, surface climate, and atmospheric circulation in California. *Clim. Dyn.* **38**, 1017–1029. (doi:10.1007/s00382-011-1123-0)
56. Konapala G, Mishra A. 2017 Review of complex networks application in hydroclimatic extremes with an implementation to characterize spatio-temporal drought propagation in continental USA. *J. Hydrol.* **555**, 600–620. (doi:10.1016/j.jhydrol.2017.10.033)
57. Wang C, Wang Y, Wang Z, Yang X. 2025 Supplementary material from: Causal network and dynamic synchronization of urban thermal environment. Figshare. (doi:10.6084/m9.figshare.c.8039819)